

This is the accepted manuscript made available via CHORUS. The article has been published as:

Many-body effects on the capacitance of multilayers made from strongly correlated materials

S. T. F. Hale and J. K. Freericks

Phys. Rev. B **85**, 205444 — Published 24 May 2012

DOI: [10.1103/PhysRevB.85.205444](https://doi.org/10.1103/PhysRevB.85.205444)

Many-body effects on the capacitance of multilayers made from strongly correlated materials

S. T. F. Hale¹ and J. K. Freericks¹

¹*Department of Physics, Georgetown University, Washington, D.C 20057, USA*

(Dated: May 3, 2012)

Recent work by Kopp and Mannhart¹ on novel electronic systems formed at oxide interfaces has shown interesting effects on the capacitances of these devices. We employ inhomogeneous dynamical mean-field theory to calculate the capacitance of multilayered nanostructures. These multilayered nanostructures are composed of semi-infinite metallic leads coupled via a strongly correlated dielectric barrier region. The barrier region can be adjusted from a metallic regime to a Mott insulator through adjusting the interaction strength. We examine the effects of varying the barrier width, temperature, potential difference, screening length, and chemical potential. We find that the interaction strength has a relatively strong effect on the capacitance, while the potential and temperature show weaker dependence.

I. INTRODUCTION

As the capabilities of electronic components increase and their sizes decrease, new ideas are needed to continue the advancements in technology². One of the fundamental electronic components is the capacitor. In its basic form it is a dielectric (κ) layer separating two conducting layers, which builds and stores charge on each conducting plane when an external potential is applied. Driving the development of high-performance capacitors is the further miniaturization of various electronic devices including metal-oxide semiconductor field-effect transistors (MOSFETs). In order to continue the trend of development, high- κ insulating materials are utilized in MOSFETs and capacitors³⁻⁵. As the size of these devices decrease, quantum mechanical effects play a greater role and complicate the trend of using higher and higher κ materials. Recent theory work by Kopp and Mannhart¹ and subsequent experimental work by Li *et al*⁶ has introduced the idea of using ultrathin strongly correlated electronic materials to produce controllable small or large capacitances instead of the traditional high- κ dielectric approach. This work builds on the growing number of possible applications of oxide interfaces⁷⁻¹⁰, as oxides forming two dimensional electron gases at the interface present a strong candidate for capacitance enhancements. The experimental work⁶ found a greater than 40% increase in the gate capacitance when the mobile electrons were nearly depleted in a $\text{LaAlO}_3/\text{SiTiO}_3$ interface. This increase is attributed to a negative compressibility of the interface electron system. Motivated by this work, we want to theoretically investigate the strong correlation effects on capacitance when the barrier is a Mott insulator.

We focus on constructing theoretical nanostructure devices consisting of ballistic metal leads on both sides of a strongly correlated electron dielectric layer. Inhomogeneous dynamical mean-field theory¹¹ (IDMFT) the theoretical framework for this work, allows for the self-consistent calculation of the properties of such devices. We use the Falicov-Kimball model¹² to govern the interaction and use a Potthoff-Nolting¹¹ technique for solving the IDMFT. We work in the static limit with no current flow, where all calculations can be carried out in equilibrium¹³.

The capacitance is calculated for various parameters, showing the strongest dependence on the interaction strength and weaker dependence on the temperature and applied potential. Two methods for calculating the capacitance are discussed in the paper, one based on the center of charge approach of Lang and Kohn¹⁴ (where one measures the total charge on the capacitor) and the other on the voltage profiles through the capacitor due to Mead¹⁵ (where one measures the voltage difference between the plates).

The general organization of the rest of this paper is as follows; in Section II, we detail the mathematical formalism and numerical issues associated with the calculation of the capacitance from the IDMFT approach. In Section III, we present numerical results of the capacitance dependence on various parameters including temperature, thickness, and dielectric screening length. We summarize the work, discussing the results and future ideas in Section IV.

II. FORMALISM

The general equation for the capacitance¹⁶, C , of two electrodes possessing charges of Q and $-Q$, separated by voltage V is

$$C = \frac{Q}{V}. \quad (1)$$

In this work, we are concerned with parallel plate capacitors; an arrangement of two-dimensional layers stacked in a sandwich configuration. Classically, the capacitance of two-plate capacitor is defined as

$$C = \frac{\epsilon_0 \epsilon_r A}{d}, \quad (2)$$

where ϵ_r is the relative dielectric constant of the material separating the plates, ($\kappa = \epsilon_0 \epsilon_r$) is the dielectric constant of the vacuum, A is the area of the plates, and d is the thickness of the dielectric. These equations assume that the charges sit on an idealized surface plane of zero thickness. This assumption does not hold in reality and the electron density distribution must be taken into account. Kohn and Lang¹⁴ showed that the effective position of the lead surface, $z_0^{R,L}$, can be calculated from a center of charge approach,

$$z_0^L = \frac{\sum_{\alpha=-\infty}^{center} z_\alpha \rho_\alpha}{\sum_{\alpha=-\infty}^{center} \rho_\alpha}, \quad (3)$$

where z_α is the position of plane α in the z -direction, and ρ_α is the charge density distribution on plane α (with $\alpha = -\infty$ being the left most plane and $\alpha = center$ being the center of the barrier region). The sum ranges over one half of the capacitor only and z_0^R is equivalently defined with sum from the center of the barrier to last plane on the right. Equation (2) is therefore modified and the capacitance per unit area of a two plate capacitor becomes

$$\frac{C_{CoC}}{A} = \frac{\epsilon_0 \epsilon_r}{(z_0^R - z_0^L)}. \quad (4)$$

For the rest of the paper we will refer to Eq. (4) as the center of charge (CoC) capacitance.

In addition to the assumption of an ideal surface charge, as the size of these devices approaches an ultrasmall regime Eq. (2) will also begin to break down. For example, a device where the effects of a single electron plays a dominate role, the calculations need to include quantum mechanics and a classical approach will not give a complete description. Quantum-mechanical effects will play an important role even before the single electron limit is reached. If the device is thin enough that the electric field is screened over a significant portion of the barrier region, there can be a noticeable reduction in the capacitance. This effect was first observed by Mead¹⁵ for thin films and gives us a modified equation¹⁷ for a thin film parallel plate capacitance per unit area;

$$\frac{A}{C_{VP}} = (d/\epsilon_0\epsilon_r) \left\{ 1 + \frac{V_a - (V_R - V_L)}{(V_R - V_L)} \right\}, \quad (5)$$

where V_a is the applied potential, V_L and V_R are the potentials at the left and right interfaces, respectively, with $(V_R - V_L)$ being the potential difference across the dielectric. Written in this form the modification to the geometric capacitance can be seen as the second term in the braces. We refer to Eq. (5) as the voltage profile (VP) capacitance for the remainder of this paper. A schematic representation of the two methods is shown in Fig. 1.

The C_{VP} method can be thought of as fixing the distance between the plates to the physical difference of the plate geometry and calculating the effective potentials at that separation. While the C_{CoC} method sums the total charge, Q , for the two halves and calculates an effective distance between charges. Hence, the effective charge in the VP method will not equal the total charge in the CoC method, while the distance between the plates in the CoC method will not equal the distance between the plates in the VP method unless the two results coincide. Each method has its relative strengths and relation to experiments discussed later in this paper.

Extracting physical properties from inhomogeneous multilayered nanostructures is made possible by utilizing the algorithm originally employed by Potthoff and Nolting¹¹ and later adapted by Freericks¹⁸. This so called quantum zipper algorithm reduces the complexity of the system by stacking two-dimensional translationally invariant planes, thereby building the inhomogeneity in the longitudinal third dimension (z) only. The z -coordinate remains in real space, while the x and y coordinates are Fourier transformed to wavevectors k_x and k_y , respectively, forming a mixed basis. Greek letters ($\alpha, \beta, \gamma, \dots$) are used to denote the planar index of the $x - y$ planes stacked in the z -direction. We are left with a quasi-one-dimensional problem for each two-dimensional band energy, that can be represented tridiagonally in real space and solved via the quantum zipper algorithm. The many-body equations are iterated to achieve a self-consistent solution. This Potthoff-Nolting approach is used to extract the electronic charge on each two-dimensional plane via the Green's functions¹⁹. The charges are then used in a classical calculation to find the potentials on each plane and then the local electrochemical potential. The approach is iterated until it reaches a steady state charge distribution.

We begin the calculations by defining the governing Hamiltonian for our system. The Hamiltonian involves a hopping term for the electrons and an interaction term for the sites within the barrier region. For the interaction in our numerical calculations, we employ the Falicov-Kimball model¹² which involves an interaction between spinless conduction electrons and spinless localized electrons. When the conduction electron hops onto a site already occupied by the localized electron, both electrons feel a mutual repulsion. When this correlation strength is large enough in the Falicov-Kimball model it has a Mott-like metal-insulator transition. Additionally the Falicov-Kimball model has the advantage of simplifying the solution of the IDMFT equations for this system. It turns out that the stabilization of the voltage profile under the iterative solution of the IDMFT equations is difficult, and to date has only been able to be achieved in numerical solutions that are extremely accurate, like the Falicov-Kimball model. In the second quantization formalism, the spinless Falicov-Kimball Hamiltonian¹² is,

$$\begin{aligned} H = & - \sum_{\alpha} \sum_{i,j \in plane} t_{\alpha ij} c_{\alpha i}^{\dagger} c_{\alpha j} - \sum_{\alpha} \sum_{i \in plane} t_{\alpha \alpha+1} \left(c_{\alpha i}^{\dagger} c_{\alpha+1 i} + c_{\alpha+1 i}^{\dagger} c_{\alpha i} \right) \\ & - \sum_{\alpha} \sum_{i \in plane} (\mu_{\alpha} - V_{\alpha} + \Delta V_{\alpha}) c_{\alpha i}^{\dagger} c_{\alpha i} + \sum_{\alpha} \sum_{i \in plane} U_{\alpha} c_{\alpha i}^{\dagger} c_{\alpha i} \left(w_{\alpha i} - \frac{1}{2} \right), \end{aligned} \quad (6)$$

where the first two terms of the Hamiltonian describe intraplane and interplane electron hopping, respectively, where $c_{\alpha i}^{\dagger}$ and $c_{\alpha i}$ are creation and annihilation operators on plane α and site i , respectively. The third term describes the charge reconstruction that occurs due to an externally applied potential, μ_{α} is the chemical potential on plane α , V_{α} is the potential energy on plane α due to the Coulomb interaction of the electronic charge reconstruction, and ΔV_{α} is the input applied potential on plane α . The last term is the interaction term where U_{α} represents the interaction strength on plane α , and $w_{\alpha i}$ is a classical variable that equals one if there is a localized particle at site i on plane α and zero if there is no localized particle at site i on plane α .

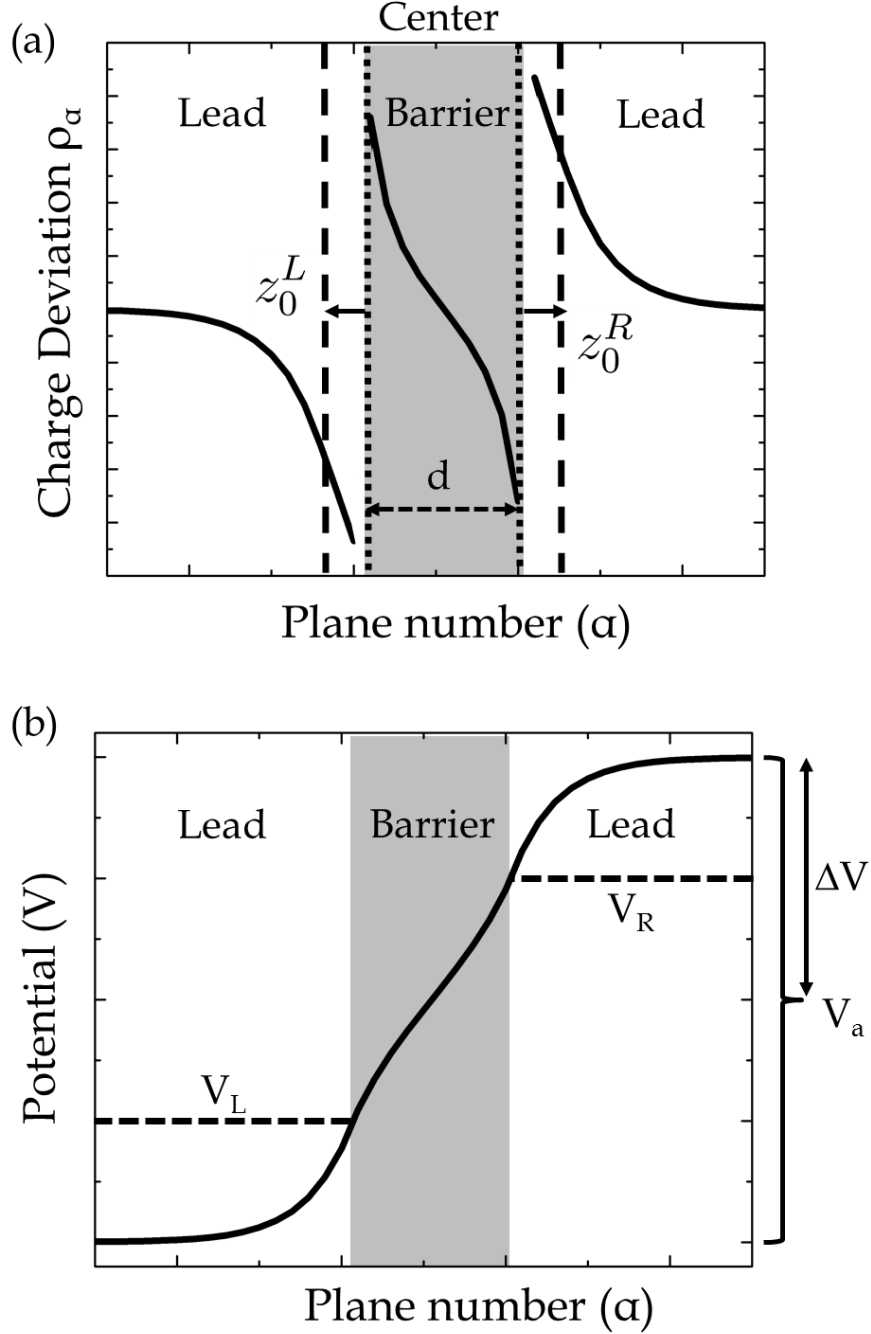


FIG. 1. Schematics of the two methods of calculation of the capacitance. Panel (a) shows the center of charge (CoC) method. The parameter z_0^L is calculated by using the charge distribution to the left of center and is shown as a dashed line. This line is shifted away from the original interface location shown as a dotted line. Similarly z_0^R is calculated by summing the charge distribution to the right of center. Figure (b) shows the voltage profile method (VP). V_L is the value of the potential at the left interface and V_R the potential at the right interface. V_a is the applied voltage which equals two times ΔV .

We will use Green's functions to solve the problem. The equilibrium Green's function, in real space, and imaginary time is defined by

$$G_{\alpha\beta ij}(\tau) = -\left\langle T_\tau c_{\alpha i}(\tau) c_{\beta j}^\dagger(0) \right\rangle, \quad (7)$$

for imaginary time τ , where T_τ represents the time ordering operator. The notation $\langle X \rangle$ denotes the trace, $\text{Tr} \exp(-\beta H) X$ divided by the partition function $\mathcal{Z} = \text{Tr} \exp(-\beta H)$, and the operators are expressed in the

Heisenberg representation $X(\tau) = \exp(\tau H) X \exp(-\tau H)$, all with respect to the Hamiltonian H . To properly express the Green's functions for the Matsubara frequencies we use a Fourier transformation

$$G_{\alpha\beta}(i\omega_n) = T \int_0^\beta d\tau e^{i\omega_n \tau} G_{\alpha\beta}(\tau). \quad (8)$$

where $T = 1/\beta$ is the temperature.

To build our model, we need to solve for the local Green's function on each plane, which we do by employing the quantum zipper algorithm¹⁸, based on the Potthoff-Nolting formalism¹¹. When solving for the local Green's functions, we use the fermionic Matsubara frequencies, $i\omega_n = i\pi T(2n+1)$. We start with the unperturbed equilibrium equation of motion (EOM),

$$\sum_\gamma G_{\gamma\beta}(i\omega_n; \mathbf{k}^\parallel) \left[(i\omega_n + \mu_\alpha - V_\alpha + \Delta V_\alpha - \epsilon_{\mathbf{k}^\parallel}^\alpha) \delta_{\alpha\gamma} + (t_{\alpha-1\alpha} \delta_{\gamma\alpha-1} + t_{\alpha+1\alpha} \delta_{\gamma\alpha+1}) - \Sigma_\alpha(i\omega_n) \delta_{\alpha\gamma} \right] = \delta_{\alpha\beta}, \quad (9)$$

where $\epsilon_{\mathbf{k}^\parallel}^\alpha = -2t_\alpha [\cos k_x + \cos k_y]$, $\mathbf{k}^\parallel = (k_x, k_y, 0)$ is defined as the transverse momentum, $\delta_{\alpha\beta}$ is the Kronecker delta function, and $\Sigma_\alpha(i\omega_n)$ is the self energy on plane α . Note that from this point on we will use the simplification that the hopping matrix elements are equal to t for nearest neighbors, $t_{\alpha+1\alpha} = t_{\alpha-1\alpha} = t_{\alpha i j} = t$ and vanish otherwise. Since the EOM has a tridiagonal form with respect to the spatial component $z(\alpha, \beta)$ it can be solved with the so-called renormalized perturbation expansion¹⁹. We solve the equation directly, for the $\beta = \alpha$ case via

$$G_{\alpha\alpha}(i\omega_n; \mathbf{k}^\parallel) = \frac{1}{i\omega_n + \mu_\alpha - V_\alpha + \Delta V_\alpha - \Sigma_\alpha(i\omega_n) - \epsilon_{\mathbf{k}^\parallel}^\alpha + \frac{G_{\alpha-1\alpha}(i\omega_n; \mathbf{k}^\parallel)}{G_{\alpha\alpha}(i\omega_n; \mathbf{k}^\parallel)} t + \frac{G_{\alpha\alpha+1}(i\omega_n; \mathbf{k}^\parallel)}{G_{\alpha\alpha}(i\omega_n; \mathbf{k}^\parallel)} t}. \quad (10)$$

We create left and right recursion relations,

$$L_{\alpha-n}(i\omega_n; \mathbf{k}^\parallel) = i\omega_n + \mu_\alpha - V_\alpha + \Delta V_\alpha - \Sigma_{\alpha-n}(i\omega_n) - \epsilon_{\mathbf{k}^\parallel}^\alpha + \frac{t^2}{L_{\alpha-n-1}(i\omega_n; \mathbf{k}^\parallel)}, \quad (11)$$

and

$$R_{\alpha+n}(i\omega_n; \mathbf{k}^\parallel) = i\omega_n + \mu_\alpha - V_\alpha + \Delta V_\alpha - \Sigma_{\alpha+n}(i\omega_n) - \epsilon_{\mathbf{k}^\parallel}^\alpha + \frac{t^2}{R_{\alpha+n+1}(i\omega_n; \mathbf{k}^\parallel)} \quad (12)$$

respectively to solve for the other values of $\alpha \neq \beta$. We start these relationships with the bulk values ($n \rightarrow \pm\infty$), which give us

$$L_{-\infty}(i\omega_n; \mathbf{k}^\parallel) = \frac{i\omega_n + \mu_{-\infty} - V_{-\infty} + \Delta V_{-\infty} - \Sigma_{-\infty}(Z) - \epsilon_{\mathbf{k}^\parallel}}{2} \pm \frac{1}{2} \sqrt{[i\omega_n + \mu_{-\infty} - V_{-\infty} + \Delta V_{-\infty} - \Sigma_{-\infty}(i\omega_n) - \epsilon_{\mathbf{k}^\parallel}]^2 - 4t^2} \quad (13)$$

and

$$R_{\infty}(i\omega_n; \mathbf{k}^\parallel) = \frac{i\omega_n + \mu_{\infty} - V_{\infty} + \Delta V_{\infty} - \Sigma_{\infty}(i\omega_n) - \epsilon_{\mathbf{k}^\parallel}}{2} \pm \frac{1}{2} \sqrt{[i\omega_n + \mu_{\infty} - V_{\infty} + \Delta V_{\infty} - \Sigma_{\infty}(i\omega_n) - \epsilon_{\mathbf{k}^\parallel}]^2 - 4t^2}. \quad (14)$$

The signs in the previous two equations are chosen to yield an imaginary part less than zero for $i\omega_n$ lying in the upper half plane, and vice versa for $i\omega_n$ lying in the lower half plane. The self-energies vanish for the ballistic metal leads used here.

To get our final expression for the Green's function, we substitute the left and right equations, Eqs. (11) and (12) respectively, into Eq. (10) to yield

$$G_{\alpha\alpha}(i\omega_n; \mathbf{k}^\parallel) = \frac{1}{i\omega_n + \mu - V_\alpha + \Delta V_\alpha - \Sigma_\alpha(i\omega_n) - \epsilon_{\mathbf{k}^\parallel}^\alpha + L_\alpha(i\omega_n; \mathbf{k}^\parallel) + R_\alpha(i\omega_n; \mathbf{k}^\parallel)}. \quad (15)$$

The local Green's functions on each plane can then be found by summing the Green's functions over the transverse momenta

$$G_{\alpha\alpha}(i\omega_n) = \int d\epsilon_{\mathbf{k}^\parallel} \rho^{2D}(\epsilon_{\mathbf{k}^\parallel}) G_{\alpha\alpha}(i\omega_n, \epsilon_{\mathbf{k}^\parallel}) \quad (16)$$

with

$$\rho^{2D}(\epsilon_{\mathbf{k}||}) = \frac{1}{2\pi^2 t a^2} K \left(1 - \sqrt{1 - \frac{(\epsilon_{\mathbf{k}||})^2}{(4t)^2}} \right) \quad (17)$$

being the $2D$ density of states (DOS), K is the complete elliptical integral of the first kind and a is the lattice constant which we set to 1 for our calculations. After calculating the local Green's functions on each plane, we use Dyson's equation to define the effective medium for each plane,

$$G_{0\alpha}^{-1}(i\omega_n) = G_{\alpha}^{-1}(i\omega_n) + \Sigma_{\alpha}(i\omega_n). \quad (18)$$

The local Green's function for the α -th plane then satisfies

$$G_{\alpha}(i\omega_n) = \frac{(1 - w_1)}{G_{0\alpha}^{-1}(i\omega_n) + \frac{1}{2}U_{\alpha}} + \frac{w_1}{G_{0\alpha}^{-1}(i\omega_n)^{-1} - \frac{1}{2}U_{\alpha}} \quad (19)$$

where w_1 is the average filling of the localized particles. Finally, we use the new local Green's functions and Dyson's equation again to find the self-energy,

$$\Sigma_{\alpha}(i\omega_n) = G_{0\alpha}^{-1}(i\omega_n) - G_{\alpha}^{-1}(i\omega_n). \quad (20)$$

This forms the basic algorithm for dynamical mean-field theory, which we now augment to determine the capacitance.

To calculate the capacitance, we need the quantum-mechanically calculated electron number density and the potential at plane α . We calculate the electronic charge on each plane by summing the Green's functions over all Matsubara frequencies on the imaginary axis, multiplied by the temperature. The electron number density at plane α satisfies

$$\rho_{\alpha} = T \sum_n G_{\alpha}(i\omega_n). \quad (21)$$

We can take advantage of the behavior of $G_{\alpha}(i\omega_n)$ at large n , which goes like $1/i\omega_n$, allowing us to regularize the Matsubara frequency summation by adding and subtracting $T \sum_n 1/[i\omega_n + \mu - \text{Re}\Sigma_{\alpha}(i\omega_{n_{\max}})]$. This gives an exact summation of the tail of the Matsubara sums and the electron number density becomes

$$\begin{aligned} \rho_{\alpha} = \frac{1}{2} + T \sum_n \left[G_{\alpha}(i\omega_n) - \frac{1}{i\omega_n + \mu_{\alpha} - \text{Re}\Sigma_{\alpha}(i\omega_{n_{\max}})} \right] \\ + \frac{1}{2} \tanh \left[\frac{\beta[\mu_{\alpha} - \text{Re}\Sigma_{\alpha}(i\omega_{n_{\max}})]}{2} \right]. \end{aligned} \quad (22)$$

To find the Coulomb potential on each plane we begin with the magnitude of the local electric field created on plane α ,

$$|\mathbf{E}| = \frac{|e| |\rho_{\alpha} - \rho_{\alpha}^{bulk}| a}{2\epsilon_0 \epsilon_{r\alpha}}. \quad (23)$$

where e is the charge of an electron, ϵ_0 is the permittivity of free space, $\epsilon_{r\alpha}$ is the relative permittivity of plane α , and ρ_{α}^{bulk} is the bulk electron density of the material of which plane α is composed. Once the total field is known for each plane, we integrate them to find the electric potentials. Since the electric field's magnitude is constant, it is straightforward to compute the Coulomb potential,

$$V_{\beta}(\alpha) = - \sum_{\alpha} (\rho_{\alpha} - \rho_{\alpha}^{bulk} - \bar{\rho}) \begin{cases} \sum_{\gamma=\alpha+1}^{\beta} \frac{1}{2} [e_{Schot}(\gamma) + e_{Schot}(\gamma-1)], & \beta > \alpha \\ 0, & \beta = \alpha \\ \sum_{\beta}^{\gamma=\alpha-1} \frac{1}{2} [e_{Schot}(\gamma) + e_{Schot}(\gamma+1)], & \beta < \alpha \end{cases} \quad (24)$$

where we define the parameter,

$$e_{Schot}(\alpha) = \frac{e^2 a}{2\epsilon_0 \epsilon_{r\alpha}}, \quad (25)$$

which characterizes the decay of the surplus charge density away from the interface. The parameter $\bar{\rho} = \sum_{\alpha} (\rho_{\alpha} - \rho_{\alpha}^{bulk})/N$ (with N the total number of self-consistent planes used in our calculations) is used to improve the convergence of our

equations and vanishes for the converged final fixed-point solution. It is worth noting that we are fixing e_{Schot} (equal in both the metal leads and barrier) and not recalculating the dielectric constant, meaning the many-body effects on the dielectric are already incorporated *a priori* in the calculation. The input e_{Schot} incorporates all contributions to the dielectric, including the bare dielectric, ion core, etc., therefore we can not directly compare our results to the geometric capacitance in Eq. (2) because we cannot isolate the different contributions to the dielectric to find the effective ϵ_r needed in the formula for the geometric capacitance.

We can now state the full algorithm used in our calculations. We start by inputting a value for the screening length (e_{Schot}), the applied potential ($\Delta V = V_a/2$), the chemical potential (μ), and the temperature (T). We begin the iterative calculations with a guess for the self-energy on each plane, usually zero or the solution to a previous calculation. Next, we use the left and right recursive equations to calculate the local Green's functions at each plane. These local Green's functions are then used to calculate the effective medium for each plane, which in turn is used to solve for the impurity Green's functions. The new impurity Green's functions are used to calculate the new self-energies which are used to feed the loop again. Additionally the impurity Green's functions are used to extract the planar filling. The planar filling is used within classical electrostatics to calculate the electric potential on each plane and in turn the contribution of the potential energy to the electrochemical potential on each plane. We average the new potentials,

$$V_\alpha^{next\ iteration} = \alpha_V V_\alpha^{old} + (1 - \alpha_V) V_\alpha^{new} \quad (26)$$

with a large damping factor α_V . The parameter α_V is usually at least 0.99 which is needed to slow the updating and prevent converging to a nonphysical solution. We iterate through these steps until the calculations converge. Due to the large damping factor, it typically takes between 1,000 and 10,000 iterations to reach convergence. In order to achieve proper convergence the errors are kept to less than one part in 10^5 , this allows for reproducibility in the algorithm ensuring the planar charge densities are accurately calculated from one iteration to the next. Keeping the error below a tolerable level has proven difficult to achieve in models other than the Falicov-Kimball model (such as the Hubbard model).

After the calculations reached a self consistent solution we can use our two methods to extract the capacitance. The CoC capacitance is calculated by summing over the extracted planar filling [Eq.(4) for both the right and left halves of the layers]. The VP capacitance is calculated by substituting the calculated electric potential at the left and right interface layers in for V_L and V_R , respectively [Eq. (5)].

III. RESULTS

All of our numerical results will be calculated at half-filling ($\mu = 0$, $\langle c_i^\dagger c_i \rangle = 1/2$, and $w_1 = \langle w_i \rangle = 1/2$). We build our model with 30 self-consistent ballistic metal planes ($U = 0$) in the leads each terminating in the bulk surrounding the dielectric layers in the center. We vary the thickness of the dielectric region from 5 to 28 planes, as seen in Fig. 2. The calculations are carried out on a simple cubic lattice allowing only nearest neighbor hopping (both interplane and intraplane hopping, t , are equal). This reduces the number of parameters in the calculations allowing focus on the properties of interest.

There are many parameters that can be varied to investigate their effects on the capacitance. For each set of parameters in our calculations, we can extract the quantum-mechanically calculated electron number density for each plane from Eq. (22), as seen in Fig. 3 (a), which plots the difference between the electron number density and the bulk electron number density through the device for various e_{Schot} . From Eq. (24) we can also plot the potentials on each plane through the device, which is shown in Fig. 3 (b), again for various values of e_{Schot} . Note how the most rapid change in the potentials occur near the interface. With the charge and the potentials known, we can calculate the capacitance for each device. Once the potentials have been calculated through the devices the capacitance is calculated from Eq. (5). Figure 3 (a) and Figure 3 (b) show that as the screening length increases the charge deviation curves become, as expected, sharper in nature.

Once we have calculated the capacitance per unit area we can compare the center of charge capacitance as defined in Eq. (4) with the voltage profile capacitance calculated from Eq. (5). Both methods of calculating the capacitance are plotted in Fig. 4 which shows that as we vary the screening length, both formulas for the capacitance follow the expected $C/A \propto (1/e_{Schot})$ behavior.

We investigate thermal effects on the capacitance by varying the temperature. Figure 5 shows that the capacitance/area falls off slightly ($\approx 4\%$) as the temperature is increased over the range of 0.1 to 0.8. In our calculation, if we take a reasonable energy scale for our system, such as a noninteracting bandwidth of 3 eV, then $t = 0.25\text{eV}$ ($U = 6$). This corresponds to a temperature range from room temperature ($T = 0.1$) to 2500K ($T = 0.8$).

Fig. 6 shows that the capacitance per unit area has a stronger dependence on the Falicov-Kimball interaction strength (U). The CoC capacitance per unit area grows faster than the VP capacitance per unit area. The CoC capacitance per unit area increases by approximately 30% across the range of interaction strengths. There is a crossover

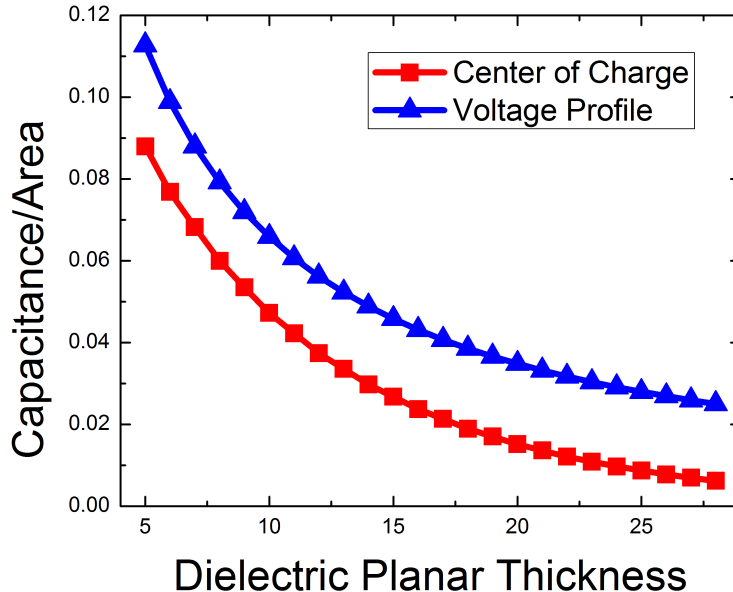


FIG. 2. (Color online) [$e_{Schot} = 0.5$, $U = 6$, $w_1 = 0.5$, $E_f = 0$, $V_a = |1|$, and $T = 0.25$] Capacitance/Area for a range of dielectric thicknesses. The Capacitance/Area displays an inverse dependence on the distance between the plates (dielectric thickness).

around $U = 7.5$ where the center of CoC becomes larger than the VP capacitance. The increase in capacitance that results from increasing the interaction strength in the barrier is due to the higher interaction strength reducing the spatial extent of the dipole layer that is formed on the inside of the dielectric region, as seen in Fig. 7.

We plot the charge deviation and potential profiles for various applied potentials (V) in Fig. 8 as well as the capacitance/area for various applied potentials in Fig. 9. The reduction in capacitance due to increasing the applied potential can be seen in Fig. 8 as the planes on either side of the dielectric layer begin to saturate and excess charge is forced further away from the interface leading to a reduction in the capacitance.

IV. CONCLUSIONS

We presented in this paper a self-consistent method for using IDMFT to calculate the capacitance of multilayered nanostructures. We also discussed the various capabilities and challenges with this many-body approach. We showed how using the quantum zipper algorithm based on the work of Potthoff and Nolting, we can calculate the electron number densities on each plane. The electron number densities were then used to calculate the electric potential on each plane from classical electrostatics. We presented two methods to calculate the capacitance, one based on a center of charge approach and the other accounting for the screening of the charges. The capacitance is calculated for various parameters, finding the strongest dependence on the interaction strength (U), 30% over the calculated range. We find a weaker dependence on temperature (5-10%) and applied potential.

We use a semiclassical approach to calculate the potential, which fixes the relation between the applied potential and the electronic charge density at a given plane. By making the dielectric a fixed parameter we cannot capture any effects on the capacitance that are not already described in Eq. (4) or Eq. (5). Fixing the dielectric in the system forces the parameter to describe the total dielectric not just the dielectric values coming from the polarizability of the ion cores. Although this limits our ability to isolate many-body effects in Eq. (4) or Eq. (5) from the geometric capacitance in Eq. (2), we are still able to examine the behavior of the model as we vary other parameters.

We calculated the capacitance via two methods, through the generated voltage profiles, C_{VP} , as well as the center of charge approach, C_{CoC} . Calculating the capacitance in these methods allows for comparison to different experimental setups. For example, if the capacitance of an experimental set up is determined by integrating the total charge required to discharge the capacitor, then comparison to the C_{CoC} method would be more appropriate because the total charge is $\sum_{\alpha} \rho_{\alpha}$ and we are not measuring the potential at the capacitor plates but between the left and right leads. On the other hand, if the experimental set up had the ability to probe the potential at the edge of the metallic plates, then the C_{VP} method is more appropriate for comparison, since we do not measure the total charge.

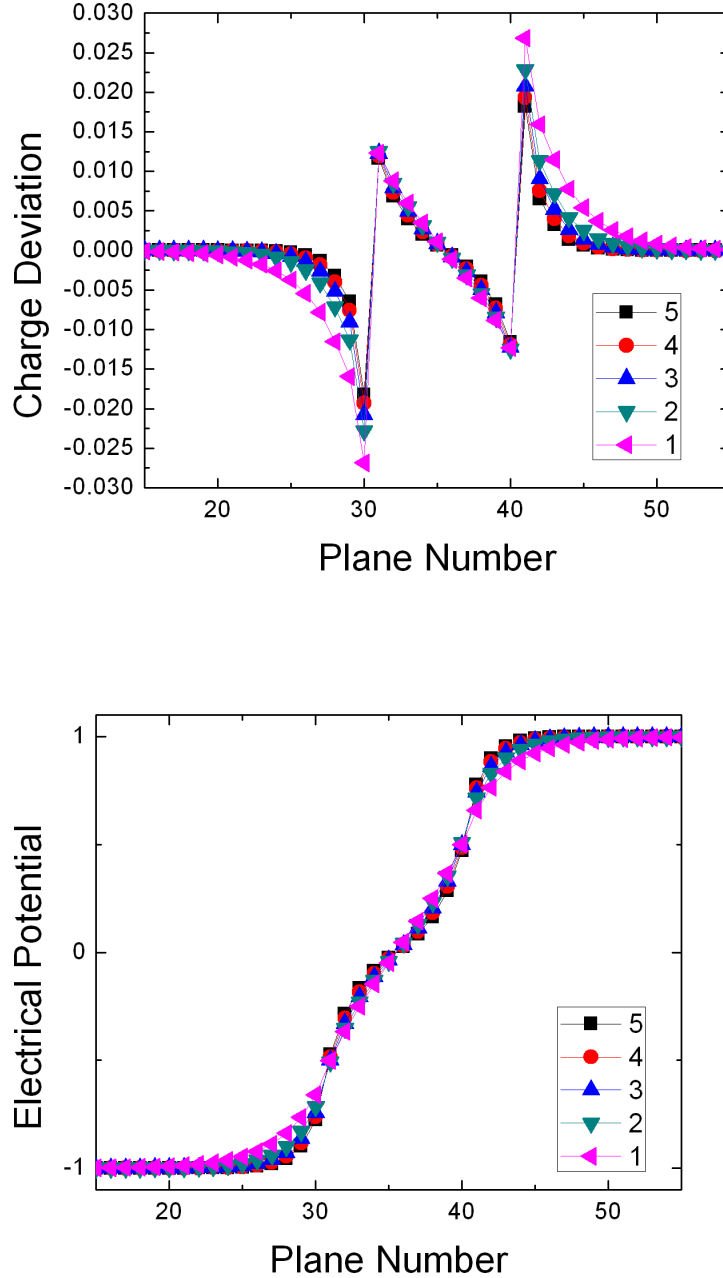


FIG. 3. (Color online) [10 dielectric planes, $U = 6$, $w_1 = 0.5$, $E_f = 0$, $V_a = |2|$, and $T = 0.25$] Charge deviations from the bulk charge (a) and the electric potential (b) plotted as a function of plane numbers for various e_{Schot} as indicated by the legends.

The ability to calculate the potential and charge profiles that incorporate many-body effects allow us to investigate any non-linear effects. The calculations for the capacitance presented in this paper were carried out in the slow limit with no current flow¹³, reproducing the inverse dependence on thickness and linear dependence on e_{Schot} . In future research moving away from half-filling would allow for the model to hopefully capture more non-linear behavior as the Falicov-Kimball model enters into a phase-separated state. Other potentially interesting and non-linear behavior can be investigated by using the Hubbard model rather than the Falicov-Kimball model, which is currently inhibited by the achievable accuracy of the required numerical calculations.

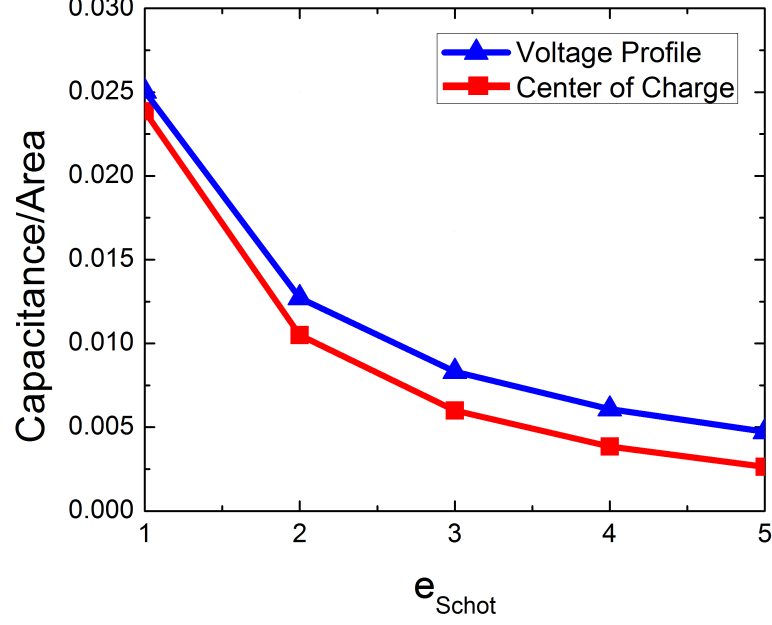


FIG. 4. (Color online) [10 dielectric planes, $U = 6$, $w_1 = 0.5$, $E_f = 0$, $V_a = |2|$, and $T = 0.25$] The capacitance per unit area plotted as a function of e_{Schot} .

The experiments see the greatest enhancements to the capacitance near the highly depleted limit, therefore by moving the Falicov-Kimball model away from half filling and forcing the model to enter a phase-separated state, we expect to see enhancements in our model. The many body effects should become more pronounced as a phase-separated state is entered.

ACKNOWLEDGMENTS

We acknowledge the support of the National Science Foundation through Grant No. DMR-1006605. J. K. Freericks acknowledges support by the McDevitt bequest at Georgetown. We also acknowledge useful conversations with Thilo Kopp and Jochen Mannhart.

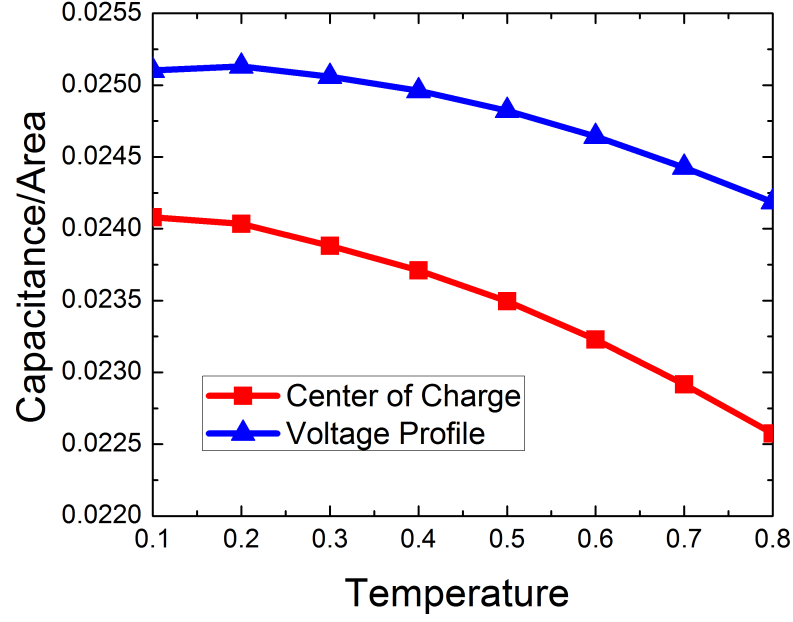


FIG. 5. (Color online) [10 dielectric planes, $e_{Schot} = 1$, $U = 6$, $w_1 = 0.5$, $E_f = 0$, and $V_a = |1|$] The capacitance per unit area plotted as a function of temperature.

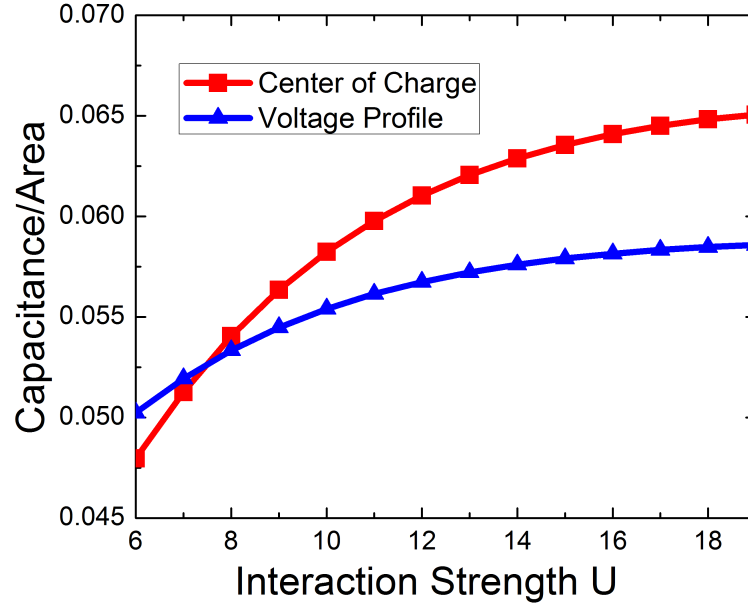


FIG. 6. (Color online) [10 dielectric planes, $e_{Schot} = 0.5$, $w_1 = 0.5$, $E_f = 0$, $V_a = |1|$, and $T = 0.25$] Capacitance per unit area for various interaction strengths U , with a crossover seen at approximately $U = 7.5$. The capacitance plateau as the charge is becomes depleted from this dielectric layer, as seen in Fig. 7

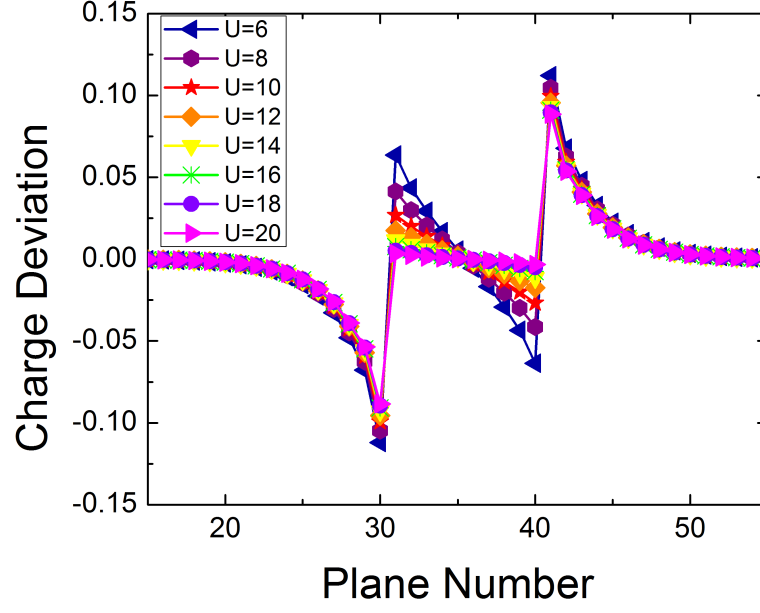


FIG. 7. (Color online) [10 dielectric planes, $e_{Schot} = 0.5$, $w_1 = 0.5$, $E_f = 0$, $V_a = |2|$, and $T = 0.25$] Charge deviations from the bulk charge plotted as a function of plane numbers for various interaction strengths (U). The charge deviation in the dielectric barrier is greatly reduced as the interaction strength is increased.

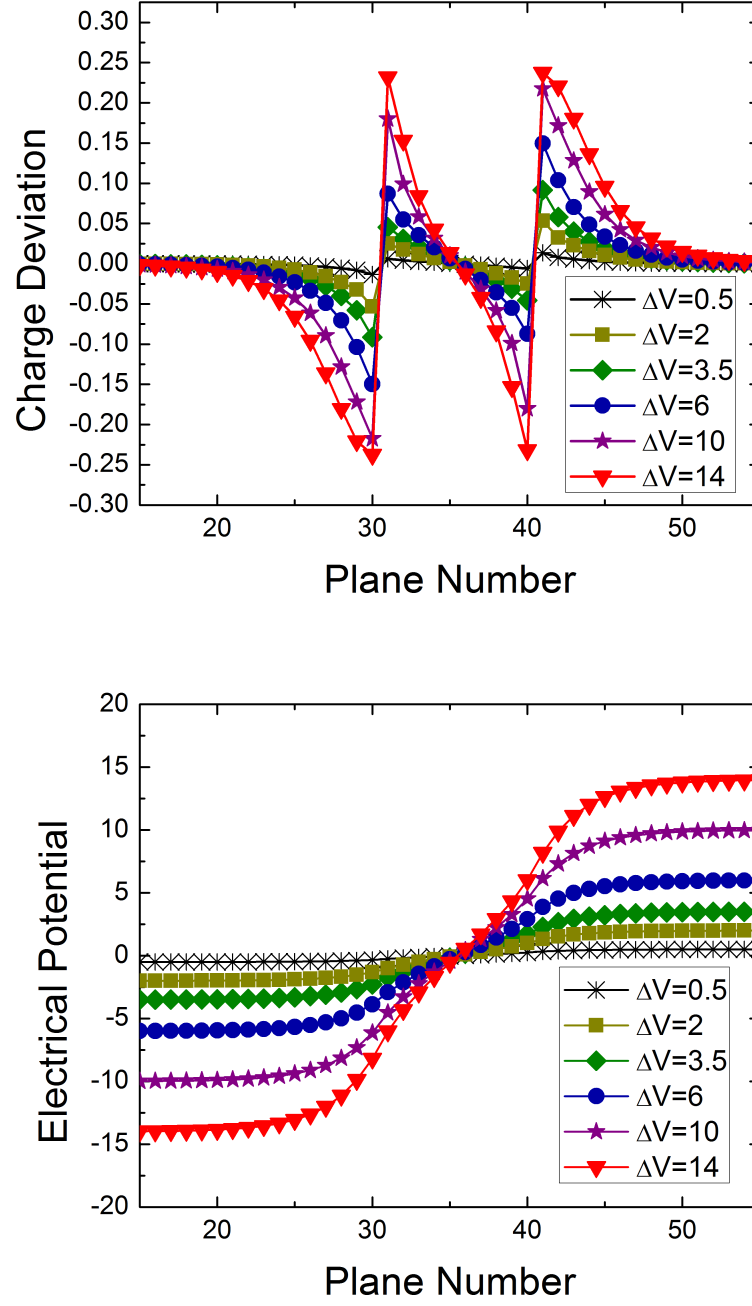


FIG. 8. (Color online) [10 dielectric planes, $e_{Schot} = 1$, $U = 6$, $w_1 = 0.5$, $E_f = 0$, and $T = 0.25$] Charge deviation from the bulk (a) and the electrical potential (b) profile for various applied potentials.

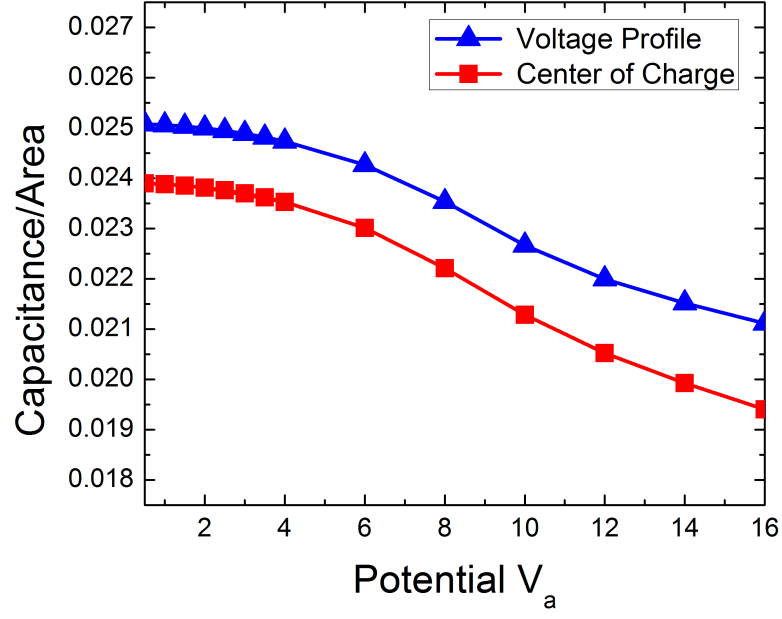


FIG. 9. (Color online) [10 dielectric planes, $e_{Schot} = 1$, $U = 6$, $w_1 = 0.5$, $E_f = 0$, and $T = 0.25$] Capacitance/Area for various applied potentials, V_a .

-
- ¹ T. Kopp and J. Mannhart, J. Appl. Phys. **106**, 064504 (2009).
 - ² J. D. Meindl, Q. Chen, and J. A. Davis, Science **293**, 2044 (2001).
 - ³ G. D. Wilk, R. M. Wallace, and J. M. Anthony, J. Appl. Phys. **89**, 5243 (2001).
 - ⁴ J. Robertson, Rep. Prog. Phys. **69**, 327 (2006).
 - ⁵ D. G. Schlom, S. Guha, and S. Datta, MRS Bull. **33**, 1017 (2008).
 - ⁶ L. Li, C. Richter, S. Paetel, T. Kopp, J. Mannhart, and R. C. Ashoori, Science **332**, 825 (2011).
 - ⁷ A. Ohtomo and H.Y. Hwang, Nature (London) **427**, 423 (2004).
 - ⁸ S. Thiel, G. Hammerl, A. Schmehl, C. W. Schneider, J. Mannhart, Science **313**, 1942 (2006).
 - ⁹ M. Breitschaft, V. Tinkl, N. Pavlenko, S. Paetel, C. Richter, J. R. Kirtley, Y. C. Liao, G. Hammerl, V. Eyert, T. Kopp, and J. Mannhart, Phys. Rev. B **81**, 153414 (2010).
 - ¹⁰ J. Mannhart and D. G. Schlom, Science **327**, 1607 (2010).
 - ¹¹ M. Potthoff and W. Nolting, Phys. Rev. B **59**, 2549 (1999).
 - ¹² L. M. Falicov and J. C. Kimball, Phys. Rev. Lett. **22**, 997 (1969).
 - ¹³ J.M. Luttinger, Phys. Rev. **135**, A1505 (1964).
 - ¹⁴ N. D. Lang and W. Kohn, Phys. Rev. B **7**, 3541 (1973).
 - ¹⁵ C. A. Mead, Phys. Rev. Lett. **6**, 545 (1961).
 - ¹⁶ J. D. Jackson, *Classical Electrodynamics* (Wiley, New York, 1975).
 - ¹⁷ H. Y. Ku and F. G. Ullman, J. Appl. Phys. **35**, 265 (1964).
 - ¹⁸ J. K. Freericks, Phys. Rev. B **70**, 195342 (2004); J. K. Freericks, *Transport in multilayered nanostructures: the dynamical mean-field theory approach* (Imperial College Press, London, 2006).
 - ¹⁹ E.N. Economou, *Green's Functions in Quantum Physics* (Springer-Verlag, Berlin, 1983).
 - ²⁰ Ling Chen and J. K. Freericks, Phys. Rev. B **75**, 125114 (2007).